Multiscale structural control of hydraulic bending in the sensitive plant *Mimosa pudica*

David A. Sleboda[1,2,*], Anja Geitmann[2], Reza Sharif-Naeini[1]

[1]Department of Physiology, McGill University

[2]Department of Plant Science, McGill University

*Corresponding Author

Article Type: Research Article

Subject Areas: Plant Biology, Physics of Living Systems

Abstract

Mechanistic studies of animal and plant motion often focus on the fundamental units of biological actuation: individual motor cells. Recent advances spanning the fields of muscle physiology and biomimetic actuation, however, reveal that important mechanical behaviors also arise at higher levels of organization, driven by the interplay of motor cells with connective tissue networks that guide and control *en masse* deformation. Here we illustrate how a paradigm of cell-driven actuation augmented by a mechanically crucial extracellular matrix is equally applicable to plant pulvini; motor organs evolutionarily distinct from but mechanically analogous to animal muscles. Using pulvini from the sensitive plant *Mimosa pudica,* we visualized anatomical sources of mechanical anisotropy at three hierarchical scales of pulvinus organization, built hydraulic physical models of observed morphologies, and analyzed 3D changes in the shapes of osmotically pressurized pulvini. We find that extracellular guidance controls the direction and extent of turgor-induced pulvinus deformation, an effect that ultimately influences the magnitude, speed, and energetic cost of pulvinus-driven motion. We discuss the relevance of these findings to ongoing work in the fields of muscle physiology and soft robotics, and we situate pulvini within a conceptual framework for understanding the design of biological motor organs generally.

Introduction

Pulvini are sites of joint-like, growth-independent motion in many plants. Visible as fleshy swellings of the bases of petioles, leaves, and individual leaflets, pulvini power active flexion and extension of leafy appendages. Pulvinus-driven movements are thought to provide a variety of adaptive benefits ranging from improving leaf temperature relations to deterring insect and grazing herbivory (Minorsky, 2019), and can occur gradually over the course of hours under the

influence of a circadian rhythm (Mayer et al., 1985) or rapidly as a thigmonastic response to touch, shaking, or wounding of a plant (e.g. Kwan et al. 2013; Song et al. 2014). Anatomically, pulvini consist of a flexible core of vasculature ringed concentrically by a thick cortex of parenchyma cells and a thin enveloping epidermis. The cortex is divided longitudinally into flexor and extensor halves, each containing parenchyma cells that act to bend the organs in flexion or extension, respectively, when turgid. Bulk movement of water from extensor parenchyma to flexor parenchyma has been observed during active bending (Tamiya et al., 1988), indicating that pulvinus deformation is a hydraulic process resulting from mass redistribution of cellular fluid within the organ. Bending is associated with efflux of K^+ and Cl^- ions from extensor cells (Kumon and Suda, 1984), offloading of sugar from vascular elements (Fromm and Eschrich, 1988a), and mass consumption of ATP (Fromm and Eschrich, 1988b), indicating that water movement is ultimately induced by active transport of ions and other osmolites to which water is attracted (Scorza and Dornelas, 2011).

While multiple theoretical models of pulvinus physiology provide insight into the biochemical mechanisms underlying hydraulic bending (e.g. Kagawa and Saito, 2000; Morillon et al., 2001; Kwan et al., 2013; Wang and Li, 2020), important functional properties crucial to a holistic understanding of plant motor biomechanics often emerge at higher levels of organization, influenced by the geometry and material properties of whole plant organs (Forterre et al., 2005, Song et al., 2014). In pulvini, polarized light microscopy suggests that the walls of hydraulic parenchyma cells are reinforced by cellulose microfibrils that selectively restrict radial cell expansion (Mayer et al., 1985). Parenchyma cells have a flattened spheroidal geometry that is conducive to deformation preferentially along the long axis of the pulvinus (Mayer et al., 1985; Koller and Zamski, 2002), and transverse wrinkles in the pulvinus surface have been identified as a morphological feature that increases longitudinal epidermis flexibility without sacrificing circumferential stiffness (Satter et al., 1970; Koller and Zamski, 2002; Song et al., 2014; Mano

and Hasebe, 2021). These structural features have great potential to influence pulvinus physiology by controlling the direction and extent of turgor-induced hydraulic deformation. Despite this, the relative contributions of cell wall ultrastructure, cell geometry, and epidermis morphology to pulvinus mechanics remain unclear, and their collective influence on the energetics of pulvinus-driven motion remains largely unexamined.

To disentangle the contributions of cell wall ultrastructure, cell geometry, and epidermis morphology to the mechanics of hydraulic pulvinus bending, we first visualized each of these structural features in a model organism for the study of rapid plant movement; the sensitive plant *Mimosa pudica*. We then used a series of osmotic perturbations to experimentally swell *M. pudica* pulvini in various states of dissection. This approach allowed us to characterize the influence of each hierarchical feature on hydraulic pulvinus deformation, but also to elucidate mechanical behaviors that emerge from cross-scale interactions between them. Additionally, we hypothesized that one collective impact of multiscale structural constraints could be a reduction in the metabolic cost of pulvinus-driven movement. To test this hypothesis, we built physical models of pulvinus structure from flexible silicone rubber and measured the mechanical pressure-volume work required to induce hydraulic bending. The energetic cost of bending was compared in two models, one with mechanically isotropic walls and one with circumferential hoop reinforcements representing structural anisotropies observed in biological pulvini. A separate physical model made of parenchyma cell morphology was built from mylar foil to explore the functional interdependence of parenchymal cell wall reinforcement and cell geometry.

Materials and Methods

Pulvinus morphology, anatomy, and ultrastructure

M. pudica plants were grown from seed in a growth chamber with a 12-hour light-dark cycle at 21-23 C and 60% humidity. Plants were watered approximately once every 3 days and fertilized monthly. The surface morphologies of primary, secondary, and tertiary pulvini, located at the bases of petioles, leaves, and leaflets, respectively, were visualized using a Hitachi TM-1000 scanning electron microscope (SEM). In preparation for SEM, freshly dissected pulvini were dehydrated in a graded series of ethanol, critical point dried, mounted on aluminum stubs with carbon double-sided tape, and sputter coated with 4 nm of gold and palladium.

To visualize cellulose orientation in the cell walls of parenchyma cells, primary pulvini were decellularized using an adapted protocol for the generation of acellular, cellulosic tissue engineering scaffolds from plant material (Adamski et al., 2018). Fresh pulvini were fixed overnight in 4% formaldehyde in 0.1 M phosphate buffer, pH 7.2 (after Kwan et al., 2013) and then bisected longitudinally using a fine razor blade under a stereomicroscope. Fixed, bisected pulvini were immersed in an aqueous solution of 3% NaOH, 5% bleach for approximately 20 hours at room temperature until they appeared uniformly white and translucent under transmitted light illumination, indicating maceration of protein material. Decellularized pulvini were then then gently rinsed in distilled water for 24 hours, dehydrated in 100% ethanol, critical point dried in liquid CO_2, mounted on aluminum stubs with carbon double-sided tape, and sputter coated with a 4 nm layer of gold and palladium. Cut faces of the bisected pulvini were imaged using an environmental scanning electron microscope (FEI Quanta 450 FE-ESEM, FEI Co.) at the McGill University Facility for Electron Microscopy Research, providing lateral views of the internal structure of the decellularized organs.

Cellulose orientation was quantified in high-magnification (~50,000-65,000x) micrographs of parenchymal cell walls using the local gradient function of the Directionality plugin in ImageJ (Liu, 1991). Orientations of identifiable structures in each image were expressed as a histogram with portion of structures observed on the Y axis and angular orientation in degrees on the X axis. All angles were expressed relative to the orientation of the vascular bundle running longitudinally through the core of each pulvinus. The peak of a gaussian curve fit to the collective histogram compiled from all micrographs provided a quantitative metric of the predominant orientation of cellulose microfibrils across samples, and the standard deviation of the gaussian curve provided a metric of histogram width, i.e., the dispersion of microfibril orientations about the predominant angle.

Osmotic perturbations

All osmotic experiments were performed on primary pulvini isolated from the bases of petioles at least two months old. Removal of proximal and distal ends of pulvini yielded approximately cylindrical sections 1000-1500 μm long and 1000-1400 μm wide. Removal of the epidermis from cylindrical pulvinus sections was then accomplished via manual skinning, or rectangular blocks of parenchyma tissue excised from the pulvinus cortex with a fine razor. For consistency, all parenchyma tissue blocks in the current study were excised from the extensor (i.e. ventral or abaxial) cortex of primary pulvini. Thin sections of parenchyma for confocal microscopy were also collected from the extensor cortex by bisecting organs with a pair of razor blades spaced by ~400 μm of double-sided tape.

Dissected pulvinus organs and tissues were soaked in aqueous mannitol solutions of varying concentration to induce osmotic swelling or shrinking. Mannitol is a biologically inert molecule and has been used previously to induce osmotic movement of water into or out of

119 hydraulic plant tissues (Mayer et al., 1985). Cylindrical sections of pulvini, cylindrical sections
120 skinned of their epidermis, and isolated blocks of parenchyma tissue were transferred through
121 graded series of osmotic mannitol baths ranging in concentration from 0 to 878 milliosmoles
122 (mOsm). Following an acclimation time of at least 30 minutes in each bath, samples were
123 imaged in both lateral and ventral views using a digital camera (Zeiss AxioCam MRc, Carl Zeiss
124 AG) mounted on a stereomicroscope (Zeiss SteREO Discovery V8, Carl Zeiss AG). Individual
125 hydraulic parenchyma cells in thin slices of parenchyma were imaged with a laser scanning
126 confocal microscope (LSM710, Carl Zeiss AG) in osmotically neutral (384 mOsm mannitol) and
127 osmotically hypotonic (distilled water) baths. Thin sections were prepared for confocal
128 microscopy by staining briefly (7-9 minutes) with 0.5 mg/ml propidium iodide (PI) in osmotically
129 neutral mannitol. PI binds to cell wall pectin and is a common stain for live imaging of plant
130 anatomical features (Bidhendi et al., 2020). After staining, tissues were rinsed briefly of unbound
131 PI and then excited with a 543 nm Helium-Neon laser at 5% power. Fluorescence emission in a
132 range of 554-711 nm was captured from parenchyma cells deep to the sectioned tissue surface.
133 Cells with a fluorescing nucleus indicating penetration of PI into the cell protoplasm were
134 considered damaged by sectioning and excluded from the study. Optical sections 2.4-6.4 μm
135 thick were captured at the midlines of cells of interest, located by changing focus along the z-
136 axis until the largest apparent cell dimensions were presented in each osmotic bath.

137 Dimensions of dissected pulvini, isolated parenchyma tissues, and individual
138 parenchyma cells were measured using Image J, FIJI (Schindelin et al., 2012). Widths, lengths,
139 and heights of pulvinus preparations measured from stereomicrographs were normalized to
140 tissue dimensions measured in the most hypertonic osmotic bath employed (878 mOsm).
141 Statistically significant changes were identified via two-tailed, one sample t-tests comparing
142 normalized dimensions in the most hypertonic (878 mOsm) and most hypotonic (0 mOsm)
143 bathing solutions. The lengths, heights, widths, lateral perimeters, and frontal perimeters of

144 individual parenchyma cells measured from confocal micrographs were normalized to
145 dimensions in osmotically neutral baths, and changes between neutral and hypotonic solutions
146 expressed as percentages. Significant changes in cell dimensions were identified as those
147 significantly different from zero in a two tailed one sample t-test.

148

149 **Physical modeling**

150 To probe the relationship between anatomical constraints and the energetic cost of
151 hydraulic bending, a pair of physical models of gross pulvinus structure were built from flexible
152 silicone rubber (Dragonskin FX Pro, Smooth-On, Inc.). One model was built with approximately
153 isotropic silicone walls while the other was reinforced anisotropically by sewing thread hoop-
154 reinforcements oriented perpendicular to the bending axis of the model. Incremental removal
155 and addition of water from opposing halves of each model simulated redistribution of cellular
156 fluid across flexor and extensor halves of a pulvinus. Hydrostatic pressures developed within
157 models were monitored via pressure gauges (DS-9192 Aneroid Sphygmomanometer Gauge,
158 Prima Care Medical Supplies) connected in series with each model half, and changes in model
159 bending angle were measured from photographs using ImageJ. Mechanical pressure-volume
160 work expended moving fluid and deforming silicone model chambers was calculated as the
161 integral of hydrostatic pressure as a function of volume change. Total pressure-volume work
162 involved in model deformation was calculated as the sum of work done on expanding halves of
163 models during both bending and returning motions, in which models flexed away from and then
164 extended back towards an initial neutral position. This method of total expansion work
165 quantification was chosen because it encompasses all of the mechanical energy loaded into
166 models during one complete cycle of motion, accounting for work done on expanding model
167 halves as well as any contractile work resulting from release of elastic strain energy stored
168 temporarily in stretched silicone walls.

To investigate the contribution of parenchyma cell geometry to anisotropic deformation, a simple model of parenchyma cells was built from heat-sealable mylar foil sheets (Mylar foil bags, Mequer). Eight foil cells with hexagonal polyhedral geometries were assembled and connected in series through their broad faces, approximating the organization of parenchyma cell files in a pulvinus. Foil cells were pneumatically continuous and could be pressurized or depressurized via addition or removal of compressed air. Foil cells were cycled through repeated cycles of expansion and contraction, and the impact of deformation on the structural integrity of the cells observed.

Results

Structural specializations associated with longitudinal flexibility are present across hierarchical spatial scales in *M. pudica* pulvini

Morphological, anatomical, and ultrastructural analyses verified that structural anisotropies were present across hierarchical scales of organization in the sensitive plant *Mimosa pudica*. Across primary, secondary, and tertiary pulvini, epidermal cells enveloping the pulvinus surface were approximately cylindrical in shape with long axes oriented perpendicular to the pulvinus long axis (Fig. 1b,c,d). Perpendicularly oriented epidermal cells were restricted to the immediate regions of pulvini, with neighboring regions of epidermis displaying parallel orientations of cells more typical of elongate plant shoots (Fig. 1e). In accordance with observations of surface wrinkles in live pulvini (Song et al., 2014), surface wrinkles in samples prepared for SEM were oriented predominantly parallel to epidermal cells, i.e., transverse to the pulvinus long axis. Surface wrinkles were confined exclusively to the surfaces of pulvini, and were not apparent on neighboring surfaces of stems, petioles, or leaflets.

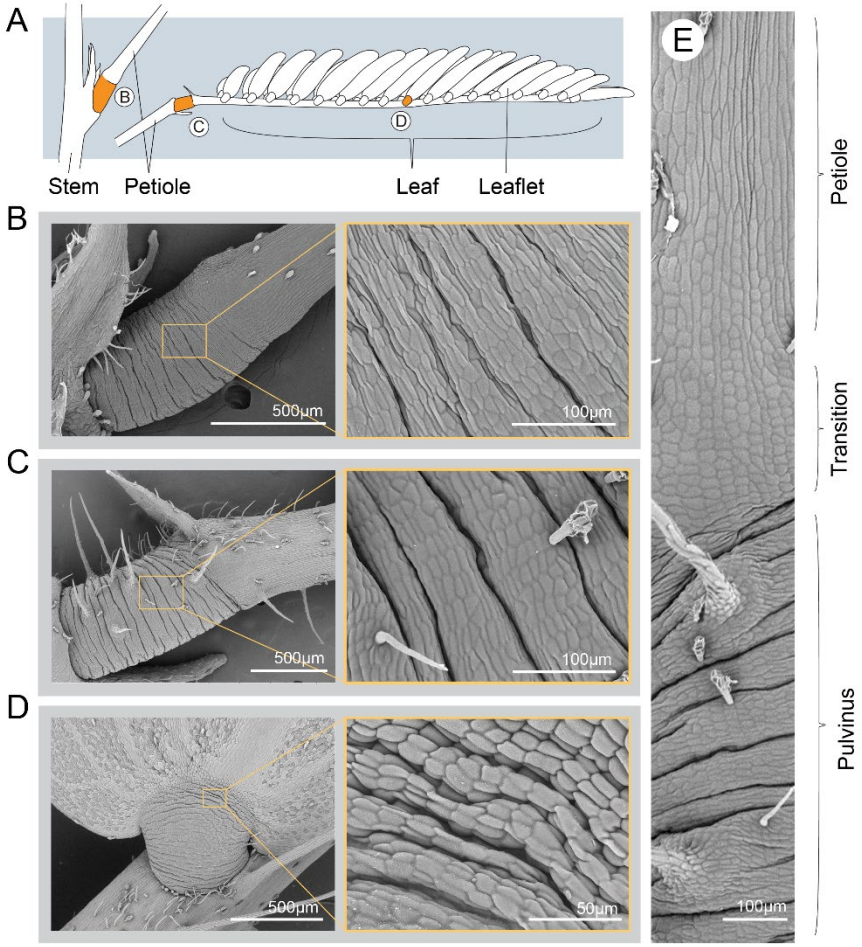

Figure 1: Epidermal cells are oriented perpendicular to the pulvinus long axis and associated with transverse surface wrinkles. [A] Line drawing depicting the locations of primary (B), secondary (C), and tertiary (D) pulvini of *Mimosa pudica*. [B,C,D] Scanning electron micrographs of pulvinus surfaces identified in [A]. Inset micrographs show epidermis architecture at higher magnifications. Epidermis cells bounding pulvini are roughly cylindrical in shape and oriented perpendicular to the long axes of organs. Wrinkles in the epidermis form preferentially parallel to the long axes of epidermis cells. [E] Epidermis cell orientation transitions from perpendicular in the region of the pulvinus to parallel in the region of the petiole (note that the organ long axis is oriented vertically in panel E).

High magnification scanning electron microscopy allowed visualization of individual cellulose microfibrils at the inner surface of parenchymal cell walls. Cellulose microfibrils were aligned primarily dorso-ventrally in the plane of the wall (Fig. 2c,d) with a predominant microfibril orientation of 82.5° ± 29.1° (mean ± SD) relative to the orientation of nearby vasculature (Fig. 2e). Microfibrils were densely arranged, with gaps between adjacent fibrils visible only at the highest magnifications employed.

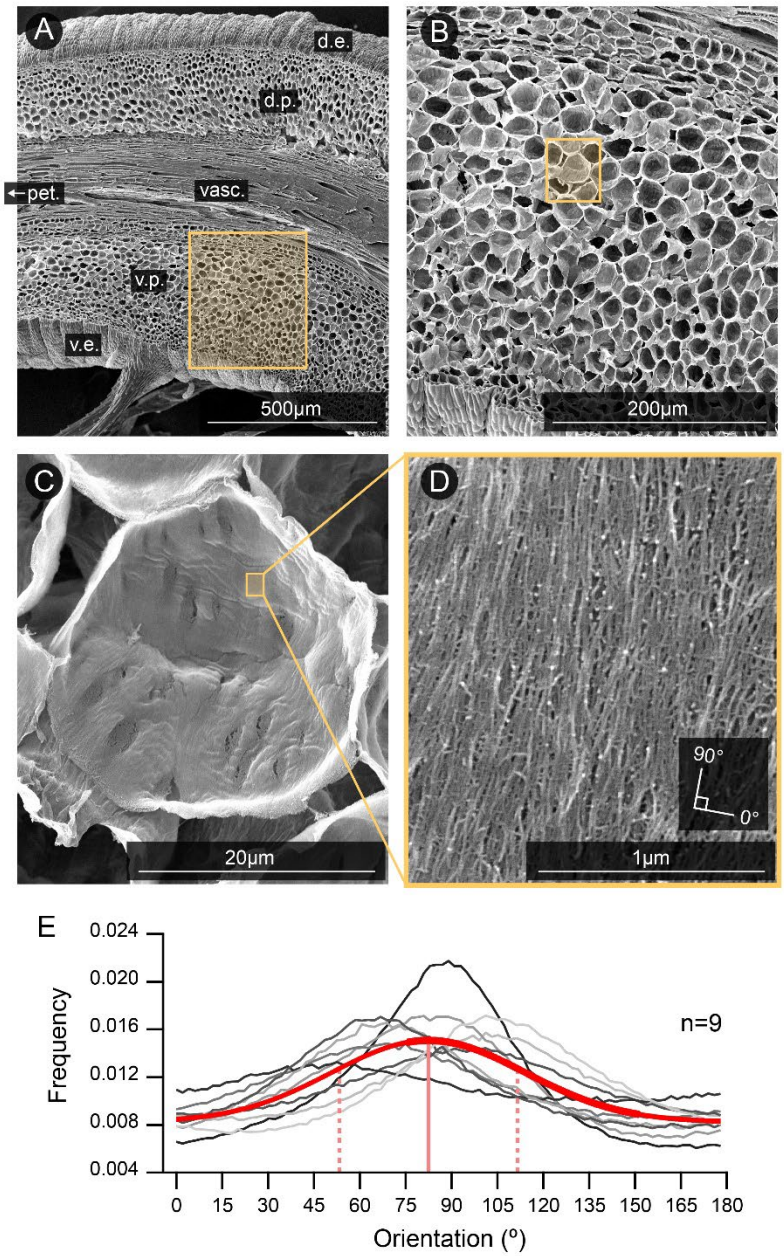

Figure 2: Cellulose microfibrils reinforcing parenchymal cell walls are oriented perpendicular to the pulvinus long axis. [A] Scanning electron micrograph showing a lateral view of a longitudinally bisected primary pulvinus. Protoplasts have been removed chemically to reveal cell wall architecture. Labels indicate dorsal (adaxial) epidermis (d.e.), dorsal parenchyma (d.p.), vasculature (vasc.), ventral (abaxial) parenchyma (v.p.), and ventral epidermis (v.e.). Organ is oriented with petiole (pet.; not visible) left of the frame. [B] Magnified view of the highlighted region in A showing ventral parenchyma bounded by vasculature and ventral epidermis. [C] Magnified view of the highlighted region in B showing the inner face of one parenchymal cell wall. [D] High magnification view of the highlighted region in C showing cellulose microfibrils running primarily dorso-ventrally in the plane of the cell wall. Fiber angles are described relative to the long axis of nearby vasculature (defined as 0°) with 90° indicating a perpendicular orientation. [E] Histograms showing distributions of fiber orientations in 9 cells from 4 pulvini. Each gray trace shows the distribution of fiber angles in a high magnification scanning electron micrograph similar to D. A gaussian curve (solid red trace) fit to all histograms indicates a predominant fiber orientation of 82.5 degrees (solid vertical line) with a standard deviation of ± 29.1 degrees (dotted vertical lines). Source data file provides tabulated histogram values.

222 **Osmotic swelling occurs anisotropically across scales of pulvinus organization**

223 Osmotic swelling experiments revealed the influence of structural specializations on the
224 mechanical behavior of *M. pudica* pulvini. Imposed osmotic swelling resulted in anisotropic
225 deformation of pulvinus tissues and cells at all hierarchical levels studied. Across a graded
226 series of osmotic baths ranging from 0 to 878 mOsm, cylindrical sections of pulvinus organ with
227 an encompassing epidermis (Fig. 3c) displayed a 15.26 ± 2.75% (mean ± standard deviation
228 (SD), $p < 0.01$) change in length without significant changes in either width (1.74 ± 1.83%, $p =$
229 0.11) or height (1.02 ± 2.42%, $p= 0.10$). Cylindrical pulvinus sections skinned of their epidermis
230 (Fig. 3d) varied in length 17.70 ± 4.26% ($p < 0.01$), increased marginally in width (2.91 ± 1.98%,
231 $p < 0.01$), and displayed increased variation in height (7.80 ± 8.55%, $p = 0.05$). Isolated blocks
232 of parenchyma tissue dissected free of epidermis and vasculature (Fig. 3e) changed in length
233 26.16 ± 3.15% ($p < 0.01$) without statistically significant changes in either width (-1.39 ± 2.40%,
234 $p = 0.26$) or height (3.76 ± 5.75%, $p = 0.22$). The increased variation in the height of cylindrical
235 organ sections skinned of their epidermis was attributable to a tendency for elongating
236 parenchyma tissues to bow dorsally and ventrally away from the stiff central vasculature of the
237 pulvinus organ. This bowing resulted in skinned pulvinus sections adopting spindle-shaped
238 lateral profiles reminiscent of rugby or American footballs when swollen osmotically (Fig. 3f and
239 Fig. 3- Video 2). Isolated blocks of parenchyma tissue dissected free of their anatomical context
240 displayed the largest changes in length of all pulvinus preparations studied, supporting the
241 notion that the stiff central vasculature resists longitudinal expansion of the pulvinus.
242

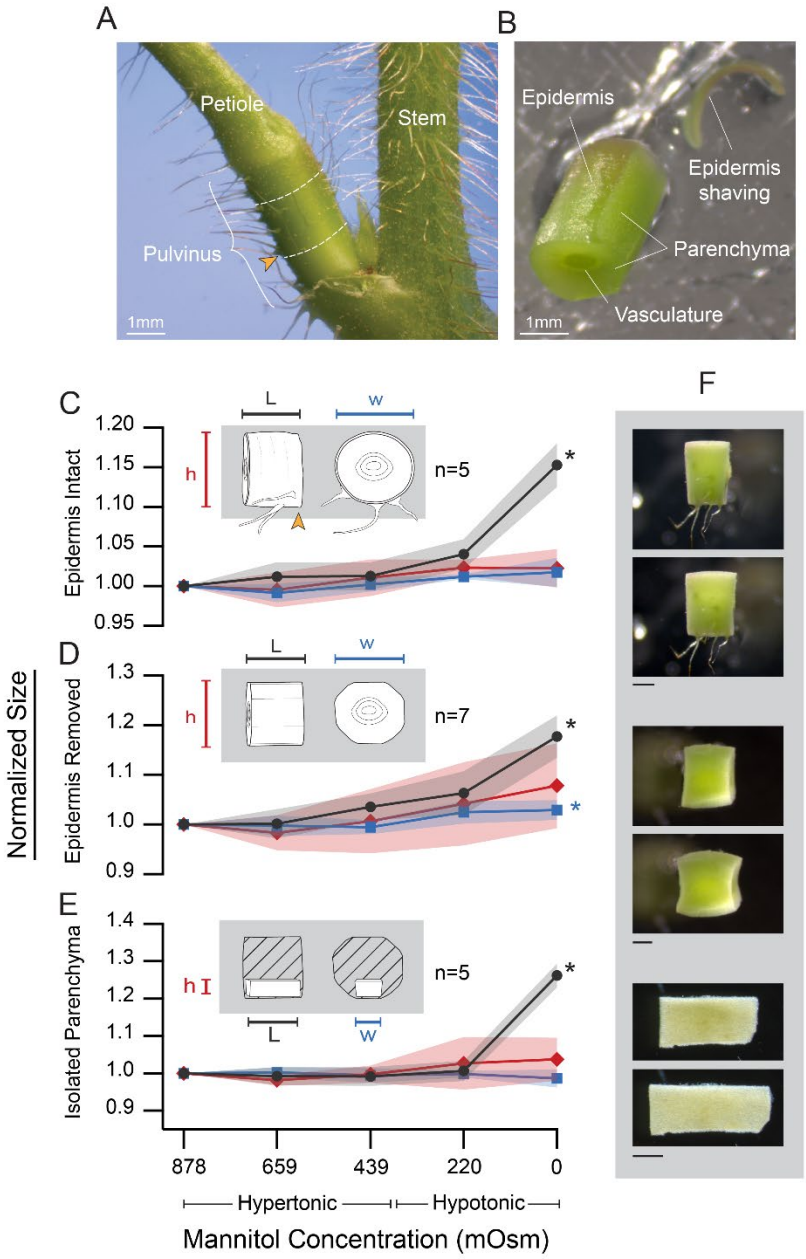

Figure 3: Nonuniform osmotic swelling of pulvini reveals multiscale control of hydraulic deformation. [A] Lateral view of an intact *Mimosa pudica* primary pulvinus with flanking leaves removed. Dashed white lines illustrate cross-sectional cuts used to isolate a cylindrical section of pulvinus. Orange arrowheads in A and C indicate proximal, ventral corner of section. [B] Isolated cylindrical section of pulvinus with epidermis partially removed to illustrate skinning technique. [C, D, E] Effect of graded osmotic bathing solutions on the length (L, black circles), cross-sectional width (w, blue squares), and height (h, red diamonds) of excised pulvinus sections. Inset line drawings depict dimensions and typical morphologies in lateral and cross-sectional views. Graph markers are means ± SD normalized to tissue dimensions in the most hypertonic bathing solution (878 mOsm). Asterisks denote values significantly different from 1.0 in the most hypotonic bathing solution (0 mOsm). [C] Isolated pulvinus sections expand longitudinally in increasingly hypotonic bathing solutions with negligible change in width or height. [D] Sections manually skinned of their epidermis expand primarily in length but display a small increase in width and increased variability in height. [E] Isolated blocks of parenchyma tissue expand longitudinally with negligible change in width or height. Sample sizes (n) for each condition are noted beside inset illustrations. [F] Representative images illustrating shape changes of pulvinus sections in each state of dissection. Upper and lower images of each pair display sample shape in hypertonic and hypotonic baths, respectively. Scale bars 500 µm. Associated videos show timelapses of osmotic deformations. Source data file provides tabulated dimensions in each osmotic condition.

The bias towards longitudinal deformation displayed by pulvinus organ sections and tissues persisted at the level of individual pulvinus parenchyma cells. The geometries of individual parenchyma cells were observable in both scanning electron micrographs of macerated pulvini (Fig. 2) and confocal micrographs of live parenchyma tissue (Fig. 4). Parenchyma cells were polyhedral spheroids approximately hexagonal in cross section. The lateral shape of live parenchyma cells was strongly dependent on the concentration of the osmotic solution in which they were maintained. In isotonic solution, cells were typically flattened slightly along their longitudinal axes; similar in shape to lentils with broad faces oriented perpendicular to the pulvinus long axis. Individual parenchyma cells (Fig. 4a) visualized within blocks of parenchyma transferred from osmotically neutral (384 mOsm) to osmotically hypotonic (0 mOsm) bathing solutions displayed a marginal change in height of 1.78 ± 2.99% (mean ± SD, $p < 0.01$), did not change significantly in width (-0.56 ± 1.88%, $p = 0.13$), but displayed a relatively large increase in length of 14.48 ± 5.07% ($p < 0.01$; Fig. 4b). Measurements of frontal and lateral cell perimeters revealed anisotropy in the amount of cell wall distension that occurred during osmotic expansion. Lateral cell perimeter, measured parallel to the organ long axis, increased 6.87 ± 3.10% ($p < 0.01$) while frontal cell perimeter, measured in cross section perpendicular to the organ long axis, changed only marginally (0.96 ± 1.41%, $p < 0.01$). Following transfer to hypotonic bathing solutions, lateral cell profiles extended without changes in cross-sectional shape, indicating deformation of longitudinally flattened cells towards more perfectly spherical polyhedral geometries under increased turgor.

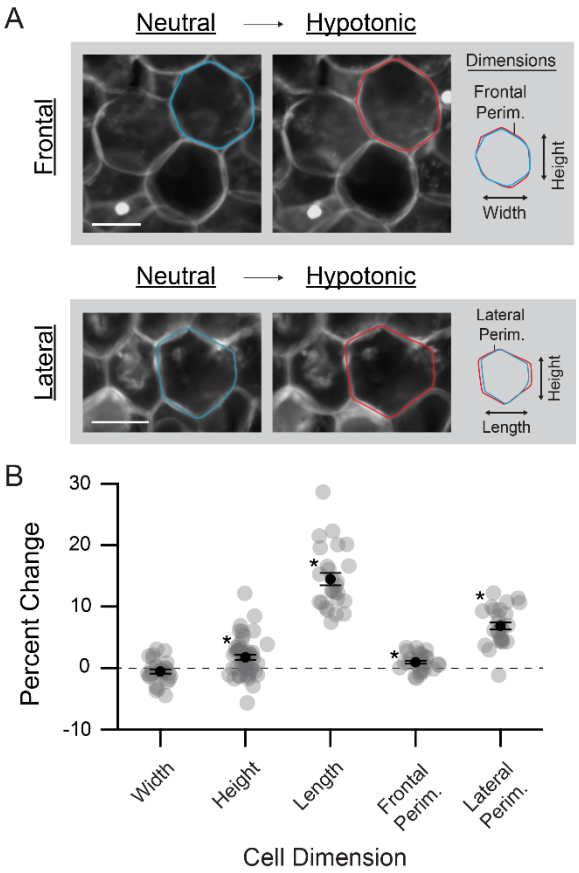

Figure 4: Nonuniform osmotic swelling of pulvinus parenchyma cells reveals mechanical anisotropy in the cell wall. [A] Confocal micrographs of parenchyma tissue imaged in osmotically isotonic (384 mOsm) and hypotonic (distilled H_2O) bathing solutions. Representative micrographs show cell morphology as seen in frontal and lateral views. All scale bars 20 µm. Inset line drawings illustrate changes in cell shape between osmotic solutions. [B] Effect of osmotic swelling on frontal and lateral dimensions of 53 cells measured over 8 experimental trials. Gray dots represent percent changes in cell dimensions following transfer from neutral to hypotonic bath. Black markers represent means ± standard errors. Asterisks denote percent changes significantly different from zero ($p<0.05$). Source data file provides tabulated dimensions in each osmotic condition.

Physical models illustrate mechanisms of anisotropic deformation and their influence on energetic efficiency

Silicone models of abstracted pulvinus structure showed the potential for passive structural constraints to influence the mechanics and energetics of hydraulic bending. Silicone models of pulvini qualitatively mimicked the hydraulic motor abilities of *Mimosa pudica,* displaying long axis bending in response to redistribution of internal fluid (Fig. 5a,b). Hoop reinforcements oriented perpendicular to the model long axis inhibited radial expansion of silicone walls and reduced the volume of fluid required to effect bending motion (Fig. 5d). Fluid pressures developed within the reinforced silicone model were higher than those in the unreinforced models (Fig. 5e); however, the energetic cost of effecting angle change via transfer of pressurized fluid across model chambers was ultimately lower in the reinforced model (Fig. 5f). Total energy input to complete one cycle of motion was 51.3 mJ for 23 degrees of bending of the unreinforced model (~2.2 mJ per degree of bending), compared to 29.7 mJ for 29 degrees of bending of the reinforced model (~1.0 mJ per degree of bending).

Foil models of abstracted parenchyma cells illustrated the influence of cell geometry on anisotropic swelling behavior. Foil models were composed of mechanically isotropic and inextensible walls. Though their walls lacked directional reinforcements, the models qualitatively mimicked the anisotropic expansion of parenchyma tissue through purely geometrical means. When pressurized internally, polyhedral, disk-shaped cells expanded longitudinally with negligible radial expansion (Fig. 6b). It was noted, however, that the inextensible foil cells were prone to kinking at their perimeters when pressurized internally, typically resulting in rupture of the model cells following repeated cycles of expansion and contraction (Fig. 6c).

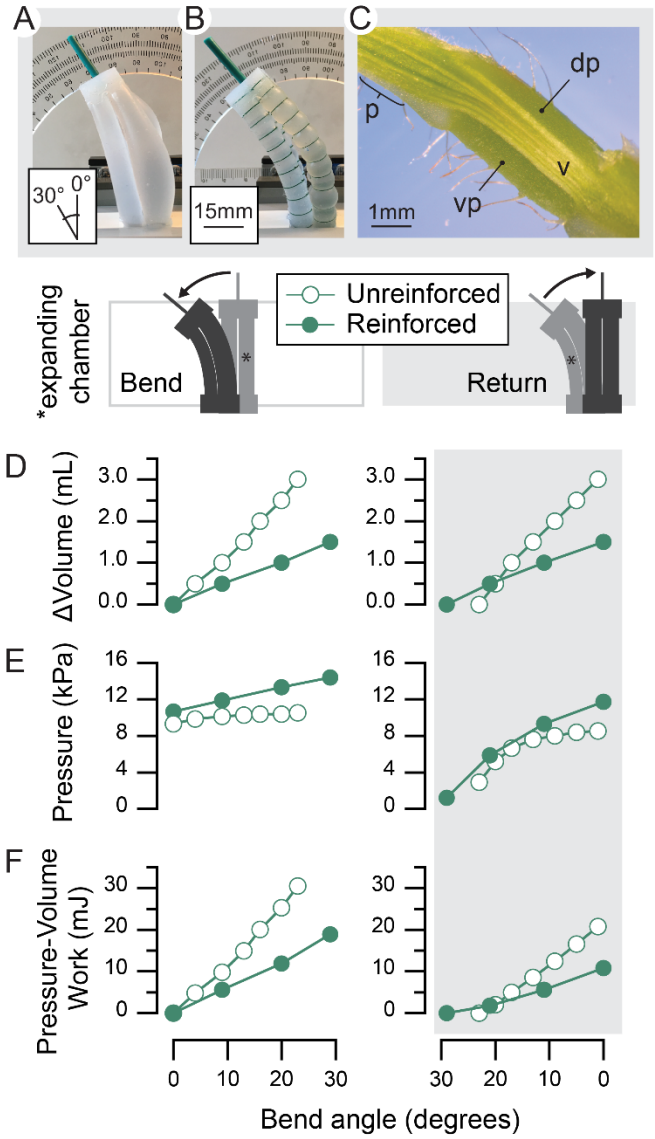

Figure 5: Physical models of gross pulvinus structure illustrate the influence of shape constraints on hydraulic and energetic bending efficiencies. [A] An abstracted physical model of a pulvinus made of flexible silicone rubber. Transfer of water from one half of the model to the other causes long-axis bending. [B] Sewing thread hoop reinforcements prevent radial expansion of pressurized model chambers. [C] Lateral view of a longitudinally bisected primary pulvinus organ. Opposing silicone chambers of each model represent dorsal (dp) and ventral (vp) parenchyma cell groups, respectively. Pulvinus vasculature (v) and petiole (p) indicated for clarity. [D, E, F] Comparison of fluid volume, pressure, and work required to effect a change in bending angle in an unreinforced (open circles) and a hoop-reinforced (filled circles) physical model. Graphs in left-hand column describe bending phase of motion for each model, while graphs in shaded right-hand column describe return phase of motion. Asterisks in inset line drawings indicate expanding halves of models in each movement phase. [D] The volume of fluid required to effect angle change is reduced in the reinforced model relative to the unreinforced model during both bend and return motions. [E] Fluid pressures measured from expanding model compartments are elevated in the reinforced model. [F] Mechanical work (the integral of pressure and volume changes) expended transferring water across model compartments is ultimately lower for the reinforced model during both bending and returning phases of motion. Associated videos show models bending hydraulically.

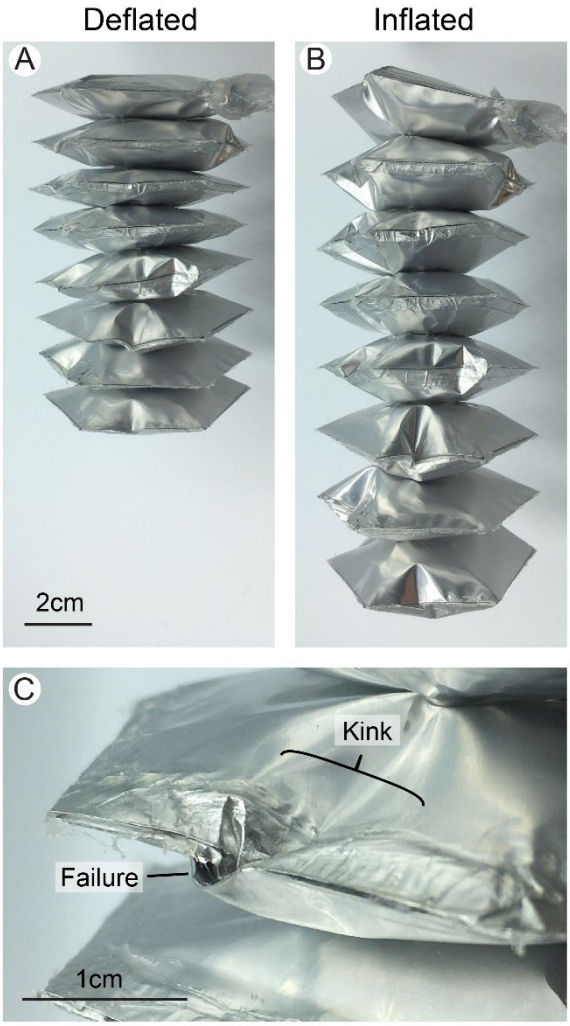

Figure 6: A mylar foil model of parenchyma cells demonstrates the influence of cell geometry on mechanical anisotropy. [A] The model is composed of eight flattened, hexagonal cells connected serially. Foil cell walls lack directional reinforcements and are inextensible and materially isotropic. [B] When pressurized internally, cells extend longitudinally with negligible change in radius. [C] Kinks formed in inextensible cell walls result in material failure and loss of pressurization following repeated cycles of expansion and contraction. Associated video shows pneumatic expansion of the model.

Discussion

The hydraulic nature of pulvinus-driven movement has been recognized since the 1800s and is discussed in Darwin's *The Power of Movement in Plants* (Darwin and Darwin, 1880). However, a holistic understanding of the mechanisms by which pulvini transform non-directional cellular turgor pressures into anisotropic, directed movement of their parts has remained elusive. Here we demonstrate that in the pulvini of the sensitive plant *Mimosa pudica,* a suite of hierarchically arranged ultrastructural, anatomical, and morphological specializations produce mechanical anisotropy at subcellular, cellular, and tissue levels of pulvinus organization. These specializations are perpendicular orientations of cellulose microfibrils in parenchymal cell walls, longitudinally-flattened spheroidal geometries of parenchyma cells, and perpendicular orientations of epidermis cells in the region of the pulvinus. The salient finding of the current work is that concerted deformation of pulvini emerges from the cross-scale interaction of these hierarchically arranged components, rather than from the independent contributions of any individual component acting in isolation. Together, they compose a multiscale structural system that guides turgor-induced deformation across scales of pulvinus organization. The silicone physical models employed in the current study suggest that one overall impact of this multiscale guidance system is a decrease in the volume of fluid transfer required to induce hydraulic actuation; a feature that ultimately reduces the energetic cost of pulvinus-driven movement.

Functional interdependence of cell wall ultrastructure and cell geometry

Through ultrastructural analysis of parenchyma cell walls, we observed cellulose microfibrils in parenchymal cell walls oriented predominantly transverse to the long axes of pulvini. Cellulose microfibrils are crystalline structures composed of closely packed chains of parallelly-oriented cellulose molecules (Brett, 2000) and display high tensile strengths and

397 longitudinal stiffnesses of approximately 1 GPa and 130 GPa respectively (Gibson, 2012).
398 Cellulose microfibrils function as the primary mechanical component of the plant cell wall,
399 ultimately providing the tensile strength needed to balance large intracellular turgor pressures
400 ranging from 0.4-0.8 MPa in typical hydrated plant tissues (Taiz et al., 2015) to over 1 MPa in
401 some specialized plant cells (Franks, 2003). Anisotropic patterns of cellulose reinforcement are
402 not unique to pulvini; cellulose orientation is actively controlled by the action of cellulose
403 synthase complexes that extrude cellulose microfibrils into the extracellular space (Brett, 2000),
404 and anisotropic cellulose deposition is the primary means by which mechanical anisotropy is
405 produced and maintained in plant cell walls. The interplay of intracellular pressure and cell wall
406 anisotropy ultimately governs the direction of irreversible turgor induced shape changes in
407 growing cells (Baskin, 2005) and underlies the development of complex non-spherical
408 morphologies (Bidhendi and Geitmann, 2016). Interactions between cell wall anisotropy and
409 turgor pressure have also been shown to underlie reversible deformation of certain mature plant
410 cell types. The hydraulic guard cells flanking stomatal pores, for example, are reinforced by
411 cellulose microfibrils oriented primarily perpendicular to the guard cell long axis (Galatis and
412 Apostolakos, 2004). The perpendicular orientation of microfibrils inhibits radial expansion of
413 guard cells while permitting elongation during hydraulic expansion, ultimately facilitating the
414 microscopic outward bowing of guard cells that opens the stomatal pore (Aylor et al., 1973).
415 Analogous to the effect of cellulose anisotropy in stomatal guard cells, our results verify that
416 cellulose microfibrils selectively restrict radial expansion of parenchymal cell walls in the pulvini
417 of *M. pudica*, resulting in anisotropic longitudinal cell wall deformation in response to turgor
418 change.

419 While deformation of parenchyma cell walls occurs preferentially along the long axis of
420 pulvini, our results indicate that direct stretching of the cell wall cannot account for all of the
421 longitudinal cell deformation observed in the current study. Following transfer from isotonic to

422 hypotonic bathing solution, the average length of parenchyma cells increased by 14.50 ± 5.07%
423 (mean ± SD); however, the lateral perimeters of these same parenchyma cells increased by
424 only 6.87 ± 3.10%, indicating that direct stretching of the cell wall accounts for less than half of
425 longitudinal cell deformation on average, even under the assumption that all cell wall distension
426 contributes exclusively to elongation. Geometric deformation of cells from longitudinally
427 flattened lateral profiles towards more perfectly spherical lateral profiles accounts for the
428 remaining observed longitudinal cell deformation, ultimately accounting for most of the
429 longitudinal cell deformation observed during osmotic expansion. The foil model illustrates this
430 crucial influence of cell geometry on longitudinal extensibility. Though foil cells were materially
431 isotropic and lacked directional reinforcements, they increased in length dramatically when
432 pressurized internally via a purely geometric bellows-like mechanism. This length increase
433 occurred without a corresponding increase in radius, qualitatively mimicking the deformations of
434 parenchyma cells subjected to increased turgor.

435 Foil models were capable of recapitulating anisotropic expansion; however, we observed
436 material failure in these physical models following repeated cycles of expansion and contraction.
437 Counterintuitively, inflated foil cells displayed kinking of their perimeters when pressurized
438 internally; a product of cell radii decreasing slightly and cell circumferences being drawn into
439 compression as a necessary consequence of elongation with constant surface area. Analogous
440 invaginations have been described previously in the walls of turgid plant cells and are
441 suggested to play a role in the generation of lobed cell morphologies by generating stress
442 hotspots (Bidhendi et al., 2019). In the foil models, circumferential kinks were often sites of
443 material failure and rupture, presumably resulting from repeated concentration of stress and
444 material fatigue. Extending this analogy to biological parenchyma cells, we suggest that in
445 addition to facilitating anisotropic stretching of cell walls in the longitudinal direction, the
446 flexibility of the cell wall imparted by unidirectional cellulose reinforcement is functionally

important as a means of mitigating stress concentrations that have the potential to damage constantly deforming parenchyma cells. Like those of growing plant cells, the cell walls of hydraulically deformable parenchyma must be stiff enough to withstand internal turgor pressure but not so stiff as to restrict turgor-driven deformation. Pulvinus parenchyma, however, faces the additional challenge that it must deform repeatedly over the lifetime of a plant without sustaining material damage significant enough to rupture cells. Accordingly, we suggest that both cell wall reinforcement and cell geometry are essential to the operation of *M. pudica* pulvini, as neither specialization in isolation could produce both the magnitude of cell deformation required for physiologically useful motion and the durability necessary for repetitive use.

Functional interdependence of cell anisotropy and epidermis reinforcement

Most plant stems and petioles are ensheathed in a skin of elongate epidermis cells oriented parallel to the growth axis of the organ (Kutschera, 2008). This parallel orientation of epidermal cells is a natural consequence of turgor-driven morphogenesis, in which elongated plant organs form developmentally through anisotropic expansion and elongation of the cells that compose them. Over most of their lengths, the petioles of *M. pudica* display a typical epidermis morphology of elongate cells oriented parallel to the organ long axis. In the immediate regions of pulvini, however, we observed epidermis cells oriented perpendicular to the growth axis. Cell orientation has been shown to have a direct effect on the material stiffness of plant epidermis, inducing anisotropic tensile properties and relatively lower tensile stiffness in the direction perpendicular to the orientation of epidermal cells (Bidhendi et al., 2020). Additionally, a perpendicular orientation of epidermis cells facilitates the formation of wrinkles transverse to the long axis of the pulvinus. Like wrinkles on the surfaces of mammalian finger and elbow joints, transverse wrinkles in the pulvinus epidermis provide extra surface area that can be

extended or contracted at low force (Song et al., 2014), ultimately allowing the epidermis to strain longitudinally at low force without sacrificing circumferential stiffness.

In the absence of an enveloping epidermis, we observed outward bowing of osmotically swollen parenchyma tissue away from the central axis of cylindrical pulvinus sections. This parenchymal bowing likely results from a difference in the longitudinal extensibility of parenchyma tissues and the vascular elements they surround. Isolated parenchyma tissues dissected away from the mechanical context of the pulvinus organ display a strong bias for purely longitudinal expansion; however, when coupled to a relatively stiff vasculature core in the context of an intact organ, pure longitudinal expansion along a straight line is resisted, and outward curvature of longitudinally expanding parenchyma tissue results. This phenomenon does not occur when the epidermis is present, indicating that the circumferential stiffness of the epidermis resists outward bowing of parenchyma tissues. While cell wall reinforcement and cell geometry ensure longitudinal expansion of individual parenchyma cells, the epidermis mitigates radial deformations that emerges at higher scales of tissue organization, ensuring that hydraulic expansion of parenchyma tissue *en masse* remains aligned along the long axis of the pulvinus.

Physical models provide insight into the effects of structural constraints on mechanical efficiency

The silicone physical models demonstrate the potential for circumferential reinforcements to influence the energetic cost of hydraulic bending. Bulk movement of fluid within pulvini is ultimately driven by osmotic and hydrostatic pressure gradients generated through active transport of ions and other osmolites against their concentration gradients (Scorza and Dornelas, 2011; Wang and Li, 2020). Forming and maintaining these gradients is an energy intensive process powered by hydrolyzation of ATP to ADP (Fromm and Eschrich, 1988a) and

incurs a physiologically relevant metabolic cost. *M. pudica* plants induced to fold at excessive frequency display a decreased investment in reproductive growth, indicating a reallocation of metabolic energy from reproduction to movement (Bao et al., 2018). Plants subjected to constant mechanical stimuli selectively reduce their touch response in advance of the onset of fatigue (Amador-Vargas et al., 2014; Abramson and Chicas-Mosier, 2016), indicating that behavioral adaptations have evolved to limit excessive actuation. In our silicone models, transverse sewing thread hoop reinforcements provide a mechanical means of reducing the energetic cost of movement by decreasing the volume of fluid transfer required to effect bending. Extending this analogy to biological pulvini, we suggest that anisotropic reinforcement of the parenchyma cell wall, longitudinally flattened spheroidal cell geometries, and perpendicular orientations of epidermal cells are all morphological specializations that function in concert to reduce the energetic cost of hydraulic movement. By passively restricting unproductive radial expansion, these structures reduce the volume of hydraulic fluid that must be displaced via active formation of osmotic gradients, ultimately reducing the metabolic energy that pulvinus-bearing plants must dedicate to motor functions.

Restrictions to unproductive radial expansion likely also influence the speed of pulvinus bending. Thigmonastic leaf movement in the sensitive plant *Mimosa pudica* is among the fastest movements displayed by plants, and one of the fastest purely hydraulic movements known in all of biology (Skotheim and Mahadevan, 2005). The minimum duration of any hydraulic movement will equal the maximum speed at which fluid transport can occur multiplied by the volume of fluid that must be displaced to complete the movement. In plant tissues, the maximum rates of hydraulic fluid movement are limited by the speeds at which osmotic gradients can be generated biochemically (Morillon et al., 2001) and by physical limitations to the speeds at which hydrostatic pressures can equilibrate via movement of fluid within a porous medium (Skotheim and Mahadevan, 2005; Forterre, 2013). Reducing unproductive radial bulging

presents a structural means of reducing the amount of fluid that must be transferred to induce a given degree of hydraulic bending, thus decreasing the amount of time required to induce hydraulic actuation, and ultimately increasing the speed of bending. The impressive speeds of pulvinus driven movements in sensitive plants are known to depend on exceptionally rapid solute redistribution mechanisms (Morillon et al., 2001), and here we illustrate that the evolution of structural systems that guide hydraulic deformation may be an equally crucial, but largely overlooked, aspect of rapid plant motor mechanics.

Towards a generalized framework for characterizing biological motor organs

Biological motor organs accomplish two distinct functions: they convert stored potential energy into the kinetic energy of motion, and they guide the expression of that kinetic energy towards accomplishment of a physiologically relevant motor task. In the case of a pulvinus, conversion of energy occurs at the subcellular level where chemical potential energy is converted into movement of solutes and, subsequently, water by the action of ATP-hydrolyzing membrane pumps (Lyubimova et al., 1964; Scorza and Dornelas, 2011). As shown in the current study, conversion of the resulting isotropic cell deformation into anisotropic tissue and organ deformation is then a product of a reinforcing extracellular matrix of parenchymal and epidermal cell walls. This pattern of subcellular energy transformation and extracellular structural guidance is not unique to pulvini. In vertebrate skeletal muscle, conversion of chemical potential to kinetic energy is accomplished via ATP-powered interactions between actin and myosin motor proteins housed within contractile muscle fibers (Cain and Davies, 1962; Rall, 2014). Coordination of the action of hundreds or thousands of contracting muscle fibers towards purposeful deformation of the entire organ, however, is a product of the collagenous extracellular matrix that reinforces muscle. The collagenous extracellular matrix surrounds and connects muscle fibers, ultimately linking them to in-series tendons and providing

545 a pathway for both internal and external transmission of force (Purslow, 2020). Interactions
546 between the matrix and the contractile cells it surrounds influences the speed and force of
547 active contraction (Eng et al., 2018; Sleboda and Roberts, 2020), as well as the material
548 stiffness of muscle tissue (Gindre et al., 2013; Sleboda and Roberts, 2017).

549 A paradigm of cellular energy transformers embedded in a guiding fibrous matrix
550 provides a useful framework in which to analyze both biological motor organs and engineered
551 biologically inspired actuators. Researchers studying biological motor organs and engineers
552 designing bioinspired systems can consider not only the mechanisms of energy conversion
553 employed by individual actuating elements, but also the means by which an investing matrix or
554 harnessing system facilitates coordinated action and the emergence of novel behaviors at
555 higher levels of organization. McKibben artificial muscles, for example, are a class of
556 engineered actuator that contains a pneumatically expandable tube surrounded by a sleeve of
557 braided fibers. Depending on the orientation of sleeve fibers, McKibben actuators can be made
558 to either forcibly elongate or forcefully shorten when pressurized internally (Chou and
559 Hannaford, 1996). Precise engineering of sleeve architecture has increased the complexity of
560 motions performable by McKibben-like actuators (Singh and Krishnan, 2017), and incorporation
561 of multiple McKibben actuators into an array has yielded complex automatic gearing behavior
562 not displayed by individual actuators (Azizi and Roberts, 2013). These emergent behaviors
563 represent a form of structural intelligence encoded mechanically via the coupling of an
564 increasingly complex reinforcing matrix to a simple pneumatically inflated system. Such
565 strategies provide a means of reducing the need for complex control inputs to achieve complex
566 motion, and thus are conducive to the design of engineered actuators with limited top-down
567 control and to the emergence of biomechanical systems that can operate largely in the absence
568 of direct neural control. Here we provide a natural example of this strategy. Through interaction
569 of energy-transforming hydraulic cells and structural guidance encoded in the structure of cell

570 walls and epidermis, pulvinus-bearing plants transform simple expansion and contraction of
571 hydraulic cells into rapid, repeatable, and directed movement of their parts.

572

573 **Acknowledgements**

574 We thank Youssef Chebli for help in microscope operation and helpful discussions about data
575 collection, and David Liu and S. Kelly Sears at the Facility for Electron Microscopy Research of
576 McGill University for help in microscope operation and data collection.

577

578 **Funding**

579 Funded by a Human Frontier Science Program long-term postdoctoral fellowship (LT - 000531/
580 2020).

581

582 **Competing Interests**

583 We have no competing interests to declare.

584

585 **Source Data Files**

586 Figure 2- Source Data 1: Histogram data- Tabulated Cellulose Orientations

587 Figure 3- Source Data 1: Tabulated Dimensions of Pulvinus Tissue Sections in Graded Osmotic
588 Baths

589 Figure 4- Source Data 1: Tabulated Dimensions of Individual Parenchyma Cells in Osmotically
590 Neutral and Osmotically Hypotonic Baths

591 **Videos**

592 Figure 3- Video 1: 30-minute timelapse video illustrating osmotic expansion of a cylindrical
593 section of pulvinus. Organ section is shown in lateral view.

594 Figure 3-Video 2: 15-minute timelapse video illustrating osmotic expansion of a cylindrical
595 section of pulvinus skinned of its enveloping epidermis. Note bowing of dorsal and ventral
596 surfaces. Organ section is shown in lateral view.

597 Figure 3- Video 3: 20-minute timelapse video illustrating osmotic expansion of a rectangular
598 block of parenchyma tissue. Tissue is shown in dorsal view.

599 Figure 5- Video 1: Hydraulically pressurizing one side an unreinforced pulvinus physical model.

600 Video S5: Hydraulically pressurizing one side of a pulvinus physical model reinforced by sewing
601 thread hoops.

602 Video S6: Pneumatic expansion of a foil model of serially connected parenchyma cells.

603

604 **References Cited**

605 Abramson, C. I. and Chicas-Mosier, A. M. (2016). Learning in plants: lessons from *Mimosa*
606 *pudica*. *Front. Psychol., 7*, 417. 10.3389/fpsyg.2016.00417.

607 Adamski, M., Fontana, G., Gershlak, J. R., Gaudette, G. R., Le, H. D. and Murphy, W. L. (2018).
608 Two methods for decellularization of plant tissues for tissue engineering applications. *J.*
609 *Vis. Exp.*, 135, e57586. 10.3791/57586.

610 Amador-Vargas, S., Dominguez, M., León, G., Maldonado, B., Murillo, J. and Vides, G. L.
611 (2014). Leaf-folding response of a sensitive plant shows context-dependent behavioral
612 plasticity. *Plant Ecol., 215*(12), 1445-1454. 10.1007/s11258-014-0401-4.

613 Aylor, D. E., Parlange, J. Y. and Krikorian, A. D. (1973). Stomatal mechanics. *Am. J. Bot., 60*(2),
614 163-171. 10.1002/j.1537-2197.1973.tb10213.x.
615 Azizi, E. and Roberts, T. J. (2013). Variable gearing in a biologically inspired pneumatic actuator
616 array. *Bioinspir. Biomim., 8*(2), 026002. 10.1088/1748-3182/8/2/026002.
617 Bao, T., Roy, G. and Cahill Jr, J. F. (2018). Photosynthetic opportunity cost and energetic cost
618 of a rapid leaf closure behavior in *Mimosa pudica*. *Am. J. Bot., 105*(9), 1491-1498.
619 10.1002/ajb2.1154.
620 Baskin, T. I. (2005). Anisotropic expansion of the plant cell wall. *Annu. Rev. Cell Dev. Biol., 21*,
621 203-222. 10.1146/annurev.cellbio.20.082503.103053.
622 Bidhendi, A. J., Altartouri, B., Gosselin, F. and Geitmann, A. (2019). Mechanical stress initiates
623 and sustains the morphogenesis of wavy leaf epidermal cells. *Cell Rep., 28*(5), 1237-
624 1250. 10.1016/j.celrep.2019.07.006.
625 Bidhendi, A. J., Chebli, Y. and Geitmann, A. (2020). Fluorescence visualization of cellulose and
626 pectin in the primary plant cell wall. *J. Microsc., 278*(3), 164-181. 10.1111/jmi.12895.
627 Bidhendi, A. J. and Geitmann, A. (2016). Relating the mechanics of the primary plant cell wall to
628 morphogenesis. *J. Exp. Bot., 67*(2), 449-461. 10.1093/jxb/erv535.
629 Bidhendi, A. J., Li, H. and Geitmann, A. (2020). Modeling the nonlinear elastic behavior of plant
630 epidermis. *Botany, 98*(1), 49-64. 10.1139/cjb-2019-0058.
631 Brett, C. T. (2000). Cellulose microfibrils in plants: biosynthesis, deposition, and integration into
632 the cell wall. *Int. Rev. Cytol.,* 199, 161-199. 10.1016/S0074-7696(00)99004-1.
633 Cain, D. and Davies, R. (1962). Breakdown of adenosine triphosphate during a single
634 contraction of working muscle. *Biochem. Biophys. Res. Commun., 8*(5), 361-366.
635 10.1016/0006-291X(62)90008-6.
636 Chou, C.-P. and Hannaford, B. (1996). Measurement and modeling of McKibben pneumatic
637 artificial muscles. *IEEE Trans. Robot., 12*(1), 90-102. 10.1109/70.481753.
638 Darwin, C. and Darwin, F. (1880). *The power of movement in plants*. Appleton, New York, NY.

Eng, C. M., Azizi, E. and Roberts, T. J. (2018). Structural Determinants of Muscle Gearing During Dynamic Contractions. *Integr. Comp. Biol., 58*(2), 207-218. 10.1093/icb/icy054.

Forterre, Y. (2013). Slow, fast and furious: understanding the physics of plant movements. *J. Exp. Bot., 64*(15), 4745-4760. 10.1093/jxb/ert230.

Forterre, Y., Skotheim, J. M., Dumais, J. and Mahadevan, L. (2005). How the Venus flytrap snaps. *Nature, 433*(7024), 421-425. 10.1038/nature03185.

Franks, P. J. (2003). Use of the pressure probe in studies of stomatal function. *J. Exp. Bot., 54*(387), 1495-1504. 10.1093/jxb/erg162.

Fromm, J. and Eschrich, W. (1988a). Transport processes in stimulated and non-stimulated leaves of *Mimosa pudica*. *Trees, 2*(1), 7-17. 10.1007/BF00196974.

Fromm, J. and Eschrich, W. (1988b). Transport processes in stimulated and non-stimulated leaves of *Mimosa pudica*. *Trees, 2*(1), 18-24. 10.1007/BF00196975.

Galatis, B. and Apostolakos, P. (2004). The role of the cytoskeleton in the morphogenesis and function of stomatal complexes. *New Phytol., 161*(3), 613-639. 10.1046/j.1469-8137.2003.00986.x.

Gibson, L. J. (2012). The hierarchical structure and mechanics of plant materials. *J. R. Soc. Interface, 9*(76), 2749-2766. 10.1098/rsif.2012.0341.

Gindre, J., Takaza, M., Moerman, K. M. and Simms, C. K. (2013). A structural model of passive skeletal muscle shows two reinforcement processes in resisting deformation. *J. Mech. Behav. Biomed. Mater., 22*, 84-94. 10.1016/j.jmbbm.2013.02.007.

Kagawa, H. and Saito, E. (2000). A model on the main pulvinus movement of *Mimosa pudica*. *JSME Int. J. C-Mech Sy., 43*(4), 923-928. 10.1299/jsmec.43.923.

Koller, D. and Zamski, E. (2002). The phototropic pulvinus of bean *Phaseolus vulgaris L.*-Functional features. *Plant Biol., 4*(5), 584-594. 10.1055/s-2002-35442.

Kumon, K. and Suda, S. (1984). Ionic Fluxes from Pulvinar Cells during the Rapid Movement of *Mimosa pudica L. Plant. Cell. Physiol., 25*(6), 975-979. 10.1093/oxfordjournals.pcp.a076813.

Kutschera, U. (2008). The growing outer epidermal wall: design and physiological role of a composite structure. *Ann. Bot., 101*(5), 615-621. 10.1093/aob/mcn015.

Kwan, K., Ye, Z., Chye, M. and Ngan, A. (2013). A mathematical model on water redistribution mechanism of the seismonastic movement of *Mimosa pudica*. *Biophys. J., 105*(1), 266-275. 10.1016/j.bpj.2013.06.001.

Liu, Z. Q. (1991). Scale space approach to directional analysis of images. *Appl. Opt., 30*(11), 1369-1373. 10.1364/AO.30.001369.

Lyubimova, M.N., Demianovskaya, N.C., Fedorovich, I.B., and Itomlenskyte, I.V. (1964). The part played by ATP in the motor function of the *Mimosa pudica* leaf (in Russian). *Biokhymya, 29*(4), 774-779.

Mano, H. and Hasebe, M. (2021). Rapid movements in plants. *J. Plant. Res., 134*(1), 3-17. 10.1007/s10265-020-01243-7.

Mayer, W.-E., Flach, D., Raju, M., Starrach, N. and Wiech, E. (1985). Mechanics of circadian pulvini movements in *Phaseolus coccineus L*. *Planta, 163*(3), 381-390. 10.1007/BF00395147.

Minorsky, P. V. (2019). The functions of foliar nyctinasty: a review and hypothesis. *Biol. Rev., 94*(1), 216-229. 10.1111/brv.12444.

Morillon, R., Liénard, D., Chrispeels, M. J. and Lassalles, J.-P. (2001). Rapid movements of plants organs require solute-water cotransporters or contractile proteins. *Plant Physiol., 127*(3), 720-723. 10.1104/pp.010732.

Purslow, P. P. (2020). The structure and role of intramuscular connective tissue in muscle function. *Front. Physiol., 11*, 495. 10.3389/fphys.2020.00495.

Rall, J. A. (2014). *Mechanism of muscular contraction*: Springer, New York, NY. 10.1007/978-1-4939-2007-5.

Satter, R. L., Sabnis, D. D. and Galston, A. W. (1970). Phytochrome controlled nyctinasty in *Albizzia julibrissin*. I. Anatomy and fine structure of the pulvinule. *Am. J. Bot., 57*(4), 374-381. 10.1002/j.1537-2197.1970.tb09826.x.

Schindelin, J., Arganda-Carreras, I., Frise, E., Kaynig, V., Longair, M., Pietzsch, T., Preibisch, S., Rueden, C., Saalfeld, S., Schmid, B., Tinevez, J. Y., White, D. J., Hartenstein, V., Eliceiri, K., Tomancak, P. and Cardona, A. (2012). Fiji: an open-source platform for biological-image analysis. *Nat. Methods, 9*(7), 676-682. 10.1038/nmeth.2019.

Scorza, L. C. T. and Dornelas, M. C. (2011). Plants on the move: towards common mechanisms governing mechanically-induced plant movements. *Plant Signal. Behav., 6*(12), 1979-1986. 10.4161/psb.6.12.18192.

Singh, G. and Krishnan, G. (2017). A constrained maximization formulation to analyze deformation of fiber reinforced elastomeric actuators. *Smart Mater. Struct., 26*(6), 065024. 10.1088/1361-665X/aa6dc6.

Skotheim, J. M. and Mahadevan, L. (2005). Physical limits and design principles for plant and fungal movements. *Science, 308*(5726), 1308-1310. 10.1126/science.1107976.

Sleboda, D. A. and Roberts, T. J. (2017). Incompressible fluid plays a mechanical role in the development of passive muscle tension. *Biol. Lett., 13*(1), 20160630. 10.1098/rsbl.2016.0630.

Sleboda, D. A. and Roberts, T. J. (2020). Internal fluid pressure influences muscle contractile force. *Proc. Natl. Acad. Sci. USA, 117*(3), 1772-1778. 10.1073/pnas.1914433117.

Song, K., Yeom, E. and Lee, S. J. (2014). Real-time imaging of pulvinus bending *in Mimosa pudica*. *Sci. Rep., 4*, 6466. 10.1038/srep06466.

Taiz, L., Zeiger, E., Møller, I. M. and Murphy, A. (2015). *Plant physiology and development*: Sinauer Associates, Sunderland, CT.

714 Tamiya, T., Miyazaki, T., Ishikawa, H., Iriguchi, N., Maki, T., Matsumoto, J. J. and Tsuchiya, T.
715 (1988). Movement of water in conjunction with plant movement visualized by NMR
716 imaging. *J. Biochem., 104*(1), 5-8. 10.1093/oxfordjournals.jbchem.a122421.
717 Wang, Y. and Li, H. (2020). Bio-chemo-electro-mechanical modelling of the rapid movement of
718 Mimosa pudica. *Bioelectrochemistry, 134*, 107533. 10.1016/j.bioelechem.2020.107533.

719

720 **Figure Legends (duplicated from above)**

721 Figure 1: Epidermal cells are oriented perpendicular to the pulvinus long axis and associated
722 with transverse surface wrinkles. [A] Line drawing depicting the locations of primary (B),
723 secondary (C), and tertiary (D) pulvini of *Mimosa pudica*. [B,C,D] Scanning electron
724 micrographs of pulvinus surfaces identified in [A]. Inset micrographs show epidermis
725 architecture at higher magnifications. Epidermis cells bounding pulvini are roughly cylindrical in
726 shape and oriented perpendicular to the long axes of organs. Wrinkles in the epidermis form
727 preferentially parallel to the long axes of epidermis cells. [E] Epidermis cell orientation
728 transitions from perpendicular in the region of the pulvinus to parallel in the region of the petiole
729 (note that the organ long axis is oriented vertically in panel E).

730

731 Figure 2: Cellulose microfibrils reinforcing parenchymal cell walls are oriented perpendicular to
732 the pulvinus long axis. [A] Scanning electron micrograph showing a lateral view of a
733 longitudinally bisected primary pulvinus. Protoplasts have been removed chemically to reveal
734 cell wall architecture. Labels indicate dorsal (adaxial) epidermis (d.e.), dorsal parenchyma (d.p.),
735 vasculature (vasc.), ventral (abaxial) parenchyma (v.p.), and ventral epidermis (v.e.). Organ is
736 oriented with petiole (pet.; not visible) left of the frame. [B] Magnified view of the highlighted
737 region in A showing ventral parenchyma bounded by vasculature and ventral epidermis. [C]
738 Magnified view of the highlighted region in B showing the inner face of one parenchymal cell
739 wall. [D] High magnification view of the highlighted region in C showing cellulose microfibrils
740 running primarily dorso-ventrally in the plane of the cell wall. Fiber angles are described relative
741 to the long axis of nearby vasculature (defined as 0°) with 90° indicating a perpendicular
742 orientation. [E] Histograms showing distributions of fiber orientations in 9 cells from 4 pulvini.
743 Each gray trace shows the distribution of fiber angles in a high magnification scanning electron
744 micrograph similar to D. A gaussian curve (solid red trace) fit to all histograms indicates a

745 predominant fiber orientation of 82.5 degrees (solid vertical line) with a standard deviation of ±
746 29.1 degrees (dotted vertical lines). Source data file provides tabulated histogram values.

747

748 Figure 3: Nonuniform osmotic swelling of pulvini reveals multiscale control of hydraulic
749 deformation. [A] Lateral view of an intact *Mimosa pudica* primary pulvinus with flanking leaves
750 removed. Dashed white lines illustrate cross-sectional cuts used to isolate a cylindrical section
751 of pulvinus. Orange arrowheads in A and C indicate proximal, ventral corner of section. [B]
752 Isolated cylindrical section of pulvinus with epidermis partially removed to illustrate skinning
753 technique. [C, D, E] Effect of graded osmotic bathing solutions on the length (L, black circles),
754 cross-sectional width (w, blue squares), and height (h, red diamonds) of excised pulvinus
755 sections. Inset line drawings depict dimensions and typical morphologies in lateral and cross-
756 sectional views. Graph markers are means ± SD normalized to tissue dimensions in the most
757 hypertonic bathing solution (878 mOsm). Asterisks denote values significantly different from 1.0
758 in the most hypotonic bathing solution (0 mOsm). [C] Isolated pulvinus sections expand
759 longitudinally in increasingly hypotonic bathing solutions with negligible change in width or
760 height. [D] Sections manually skinned of their epidermis expand primarily in length but display a
761 small increase in width and increased variability in height. [E] Isolated blocks of parenchyma
762 tissue expand longitudinally with negligible change in width or height. Sample sizes (n) for each
763 condition are noted beside inset illustrations. [F] Representative images illustrating shape
764 changes of pulvinus sections in each state of dissection. Upper and lower images of each pair
765 display sample shape in hypertonic and hypotonic baths, respectively. Scale bars 500 μm.
766 Associated videos show timelapses of osmotic deformations. Source data file provides
767 tabulated dimensions in each osmotic condition.

768

769 Figure 4: Nonuniform osmotic swelling of pulvinus parenchyma cells reveals mechanical
770 anisotropy in the cell wall. [A] Confocal micrographs of parenchyma tissue imaged in osmotically
771 isotonic (384 mOsm) and hypotonic (distilled H_2O) bathing solutions. Representative
772 micrographs show cell morphology as seen in frontal and lateral views. All scale bars 20 μm.
773 Inset line drawings illustrate changes in cell shape between osmotic solutions. [B] Effect of
774 osmotic swelling on frontal and lateral dimensions of 53 cells measured over 8 experimental
775 trials. Gray dots represent percent changes in cell dimensions following transfer from neutral to
776 hypotonic bath. Black markers represent means ± standard errors. Asterisks denote percent
777 changes significantly different from zero ($p<0.05$). Source data file provides tabulated
778 dimensions in each osmotic condition.

779

780 Figure 5: Physical models of gross pulvinus structure illustrate the influence of shape
781 constraints on hydraulic and energetic bending efficiencies. [A] An abstracted physical model of
782 a pulvinus made of flexible silicone rubber. Transfer of water from one half of the model to the
783 other causes long-axis bending. [B] Sewing thread hoop reinforcements prevent radial
784 expansion of pressurized model chambers. [C] Lateral view of a longitudinally bisected primary
785 pulvinus organ. Opposing silicone chambers of each model represent dorsal (dp) and ventral
786 (vp) parenchyma cell groups, respectively. Pulvinus vasculature (v) and petiole (p) indicated for
787 clarity. [D, E, F] Comparison of fluid volume, pressure, and work required to effect a change in
788 bending angle in an unreinforced (open circles) and a hoop-reinforced (filled circles) physical
789 model. Graphs in left-hand column describe bending phase of motion for each model, while
790 graphs in shaded right-hand column describe return phase of motion. Asterisks in inset line
791 drawings indicate expanding halves of models in each movement phase. [D] The volume of fluid
792 required to effect angle change is reduced in the reinforced model relative to the unreinforced
793 model during both bend and return motions. [E] Fluid pressures measured from expanding

model compartments are elevated in the reinforced model. [F] Mechanical work (the integral of pressure and volume changes) expended transferring water across model compartments is ultimately lower for the reinforced model during both bending and returning phases of motion. Associated videos show models bending hydraulically.

Figure 6: A mylar foil model of parenchyma cells demonstrates the influence of cell geometry on mechanical anisotropy. [A] The model is composed of eight flattened, hexagonal cells connected serially. Foil cell walls lack directional reinforcements and are inextensible and materially isotropic. [B] When pressurized internally, cells extend longitudinally with negligible change in radius. [C] Kinks formed in inextensible cell walls result in material failure and loss of pressurization following repeated cycles of expansion and contraction. Associated video shows pneumatic expansion of the model.